

Monte-Carlo method based simulation framework for microwave SQUID multiplexers

C. Schuster,¹ M. Wegner,^{1, a)} and S. Kempf^{1, a)}

Institute of Micro- and Nanoelectronic Systems, Karlsruhe Institute of Technology, Hertzstrasse 16, Building 06.41, D-76187 Karlsruhe, Germany

(*Electronic mail: constantin.schuster@kit.edu)

(Dated: 18 November 2022)

Performance prediction and optimization of microwave SQUID multiplexers has largely been based on simple approximate analytical models and experimental results so far. This results from the complexity of the underlying physics and the intricacy of operation and readout parameters. As a simplified description can never account for all potential effects occurring in a real device, we have developed a Monte-Carlo based simulation framework to simulate the characteristic and performance of a microwave SQUID multiplexer. Our simulation framework is a powerful tool to aid understanding and optimization of microwave SQUID multiplexers and other related devices. It includes common readout schemes such as open-loop or flux ramp modulated readout as well as the nonlinear behavior of Josephson tunnel junctions. Moreover, it accounts for the finite response time of superconducting microwave resonators with high loaded quality factors as well as the most significant noise contributions such as amplifier noise, resonator noise as well as SQUID noise. This ultimately leads to a prediction of device performance that is significantly better as compared simple analytical methods. Using the simulation framework, we discuss first steps towards a full microwave SQUID multiplexer optimization and highlight some other applications which our simulation framework can be used for.

I. INTRODUCTION

Cryogenic detectors such as superconducting transition edge sensors (TESs)^{1,2}, magnetic microcalorimeters (MMCs)^{3,4} or magnetic penetration depth thermometers (MPTs)^{5,6} have impressively proven to be among the most sensitive devices for measuring incident power or energy. For this reason, they represent the current state of the art for bolometric or calorimetric applications and various experiments strongly benefit from or even rely on the exceptional and outstanding properties of these detectors. Using an ultra-sensitive thermometer, based on superconducting (TES, MPT) or paramagnetic (MMC) materials, as well as an appropriate low-impedance readout circuit, they convert the actual input signal into a change of electrical current or magnetic flux that is continuously measured with utmost sensitivity by means of a wideband superconducting quantum interference device (SQUID)⁷.

The maturity of fabrication technology allows 'easily' building detector arrays of virtually any size. Out of these, small-scale detector arrays with up to a few tens of detectors can be readily read out with individual single-stage or two-stage dc-SQUIDs as they are used for single-channel readout. In contrast, medium-scale and particularly large-scale detector arrays necessarily demand the application of cryogenic SQUID based multiplexing techniques to address the challenging requirements related to overall cost, system complexity and the interplay between readout induced power dissipation and cooling power of the cryostat.

Existing SQUID multiplexers rely on time-division⁸,

frequency-division using MHz^{9,10} or GHz carriers¹¹⁻¹³, code-division¹⁴ or hybrid¹⁵⁻¹⁸ multiplexing schemes. Out of these, microwave SQUID multiplexing¹¹⁻¹³ appears to be best suited for the readout of large and ultra-large scale detector arrays as the bandwidth per readout channel does not necessarily have to be restricted and readout noise is to first order independent of the number of readout channels. A microwave SQUID multiplexer (μ MUX) employs transmission line or lumped element based superconducting microwave resonators as frequency encoding elements. Each resonator is capacitively coupled to a transmission line, common to all readout channels of the multiplexer, and inductively coupled to a non-hysteretic current-sensing rf-SQUID being connected to the associated cryogenic detector. Due to its parametric self-inductance, the SQUID transduces the detector signal into a change of amplitude and phase of a microwave signal continuously probing the resonance frequency of the resonator. Figure 1 shows a simplified equivalent circuit diagram of a single μ MUX readout channel based on a lumped element resonator. The resonator is formed by the parallel circuit consisting of the capacitance C and the inductance $L = L_R + L_T$. It is coupled to a transmission line with impedance Z_0 via the capacitance C_C and coupled to ground by a parasitic capacitance C_{para} . The effects of this parasitic capacitance can be described by an effective value $C_C^{\text{eff}} = (C_C^{-1} + C_{\text{para}}^{-1})^{-1}$ for the coupling capacitance. Thus, for simplicity, we will assume C_C to include the parasitic inductance going forward, rather than including C_{para} explicitly. The load inductance L_T inductively couples the resonator to the SQUID with mutual inductance $M_T = k_T \sqrt{L_T L_S}$. Here, k_T denotes the geometrical coupling factor. The SQUID comprises a closed superconducting loop with inductance L_S that is interrupted by a single unshunted Josephson tunnel junction with critical current I_c . To guarantee non-hysteretic, i.e. dispersive, operation, the SQUID hysteresis parameter is $\beta_L = 2\pi L_S I_c / \Phi_0 < 1$. A

^{a)}Also at the Institute for Data Processing and Electronics, Karlsruhe Institute of Technology, Hermann-von-Helmholtz-Platz 1, Building 242, D-76344 Eggenstein-Leopoldshafen

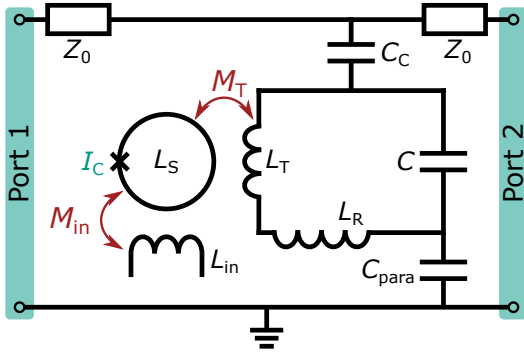


FIG. 1. Simplified schematic circuit diagram of a single readout channel of a lumped element based microwave SQUID multiplexer.

current I_{in} running through the input coil with inductance L_{in} , as caused by a detector signal, induces a magnetic flux signal $\Phi_{in} = L_{in}I_{in}$ threading the SQUID loop. In this arrangement, the resonance frequency is altered as the flux through the SQUID loop changes. The former can easily be read out by using a microwave probe tone of constant amplitude and frequency passing by the multiplexer and measuring amplitude and/or phase of the transmitted signal.

The periodicity (the period is given by the magnetic flux quantum Φ_0) of the magnetic flux dependence of the resonance frequency necessitates a method for linearising the μ MUX output signal. The most common method is flux ramp modulation (FRM)¹⁹. Here, a sawtooth-shaped current signal is injected into a modulation coil with inductance L_{mod} that is connected in series with the corresponding coils of the other channels. Moreover, it is inductively coupled to the SQUID via the mutual inductance $M_{mod} = k_{mod}\sqrt{L_{mod}L_S}$ to induce a linearly increasing magnetic flux bias. Here, amplitude I_{mod}^{max} and repetition rate f_{mod} of the modulation signal are chosen such that multiple flux quanta are induced in the SQUID loop and that the detector signal is quasi-static within a period of the flux ramp. In this case, the detector signal manifests as a phase offset in the periodic SQUID response that is continuously probed by the flux ramp signal. The relation between the amplitude of the input signal and the resulting phase offset is linear and can be easily determined by demodulation of the μ MUX output signal¹⁹.

Due to the non-linearity of the Josephson equations describing the underlying physics of Josephson junctions as well as the associated dependence of the SQUID response on the probe tone power²⁰, μ MUX characteristics are intrinsically non-linear. In combination with non-linear effects related to the finite resonator response time, the mutual dependencies of a large number of μ MUX parameters, e.g. the readout power influences the resonance frequency, noise source emerging from passive and active components of the microwave setup used for μ MUX operation as well as the complexity of the FRM readout, they lead to an intricate physical behavior prohibiting the application of analytical methods for μ MUX description and optimization. However, as the optimization of design and readout parameters is crucial for next-generation detector systems, we developed a simulation framework based

on a Monte-Carlo method to explore and optimize μ MUX behavior by means of numerical simulations.

In this paper, we describe the structure of our simulation framework. This includes a short review and discussion of the used physics models and numerical algorithms as well as a summary of the input parameters and settings that need to be specified for performing a simulation run. We then show that our simulation results are in very good agreement with expectations based on information theory as well as experimental data acquired by characterizing a lumped-element resonator based microwave SQUID multiplexer. Here, we explicitly show that our simulations describe data much better as compared to analytical models not being able to account for all mutual dependencies or non-linear effects. Finally, we outline possible areas of applications of our simulation framework. This includes an analysis of the nonlinearity between the input and output signal remaining despite the use of flux ramp modulation as well as a first step towards full μ MUX optimization. The latter is, however, not within the scope of this paper and will be presented and discussed in a future publication.

II. DESCRIPTION OF THE SIMULATION FRAMEWORK

The physics of a microwave SQUID multiplexer is governed by several implicit equations that can hardly be tackled and solved by analytical means. For this reason, we apply numerical methods to assess μ MUX characteristics and performance for a predefined set of device parameters. More precisely, we generate/calculate a time-discrete transmission time trace $S_{21,k} = S_{21}(t_k)$ with $k = 0, \dots, N-1$ and $N \in \mathbb{N}$ at equidistant points t_k in time. This time trace $S_{21,k}$ represents a discrete version of the time-dependent, complex-valued transmission parameter $S_{21}(t)$ of a single μ MUX channel as sampled in a real setup using a data acquisition system running with sampling rate $f_s = 1/(t_k - t_{k-1})$. We then analyze this artificial time trace by means of the same methods and algorithms as used for experimental data to yield, for example, a magnetic flux noise spectral density.

Figure 2 schematically depicts a flowchart outlining the general structure of our simulation framework to perform a single simulation run yielding the transmission time trace $S_{21}(t_k)$ for a given set of device and readout parameters. This time trace is afterwards analyzed using a modified Welch's method (for details see section III) to determine the magnetic flux noise spectral density. In the following, we give a short overview of the basic workflow of such a single simulation run in chronological order. In section III, we then comprehensively discuss the individual steps including all specifics and underlying equations.

A. Step 1: Generation of noise traces

The first step is the generation of quasi-random noise time traces. We include three noise sources, i.e. amplifier noise added along the entire output signal path, two-level system

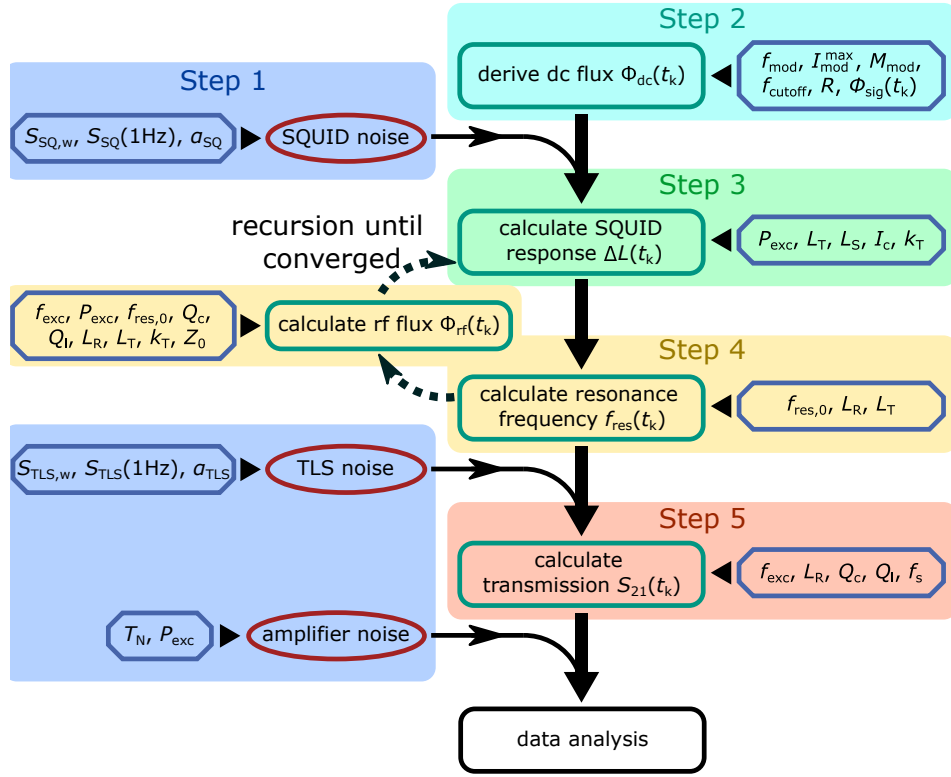


FIG. 2. Flowchart outlining the structure of the simulation framework we developed for studying μ MUX characteristics and performance by means of numerical simulations. Blue octagons represent user specified input parameters, red ovals depict noise generation and green boxes general calculations. The individual steps as well as the meaning of the different symbols and variables are explained in the main text.

(TLS) noise of the readout resonators affecting the resonance frequency as well as magnetic flux noise of the SQUID (SQ). We assume the amplifier noise to be white, i.e. frequency-independent. Its magnitude is calculated according to predefined effective noise temperature T_N of the readout system as well as the readout power P_{exc} . For both, TLS noise and SQUID magnetic flux noise, we assume the noise to be composed of a frequency-independent white and a frequency-dependent $1/f^\alpha$ -like contribution. Either noise trace is hence generated according to three input parameters $S_{i,w}$, $S_i(1\text{Hz})$ and α_i with $i \in \{\text{TLS}, \text{SQ}\}$ determining the resulting noise spectral density $S_i = S_{i,w} + S_i(1\text{Hz})/f^\alpha$. As such, $S_{i,w}$ represents the amplitude of the white noise contribution and $S_i(1\text{Hz})$ the amplitude at a frequency of $f = 1\text{Hz}$ and the exponent α of the $1/f^\alpha$ -like contribution. It is worth mentioning that changing the shape of the noise spectra of either noise contribution requires only minor modifications of the source code. So, arbitrary shapes of the noise spectra can be easily chosen.

B. Step 2: Calculation of the quasi-static magnetic flux threading the the SQUID loop

The magnetic flux Φ_{tot} threading the SQUID loop is composed of three contributions, i.e. the actual input signal Φ_{in} , the sawtooth-shaped flux ramp Φ_{mod} as well as the magnetic

flux Φ_{rf} induced by the microwave signal within the readout resonator. Out of these, the input signal and the flux ramp appear to be quasi-static as compared to the flux induced by the microwave signal. For this reason, we denote the first two contributions as 'dc-flux', though it is slowly (with respect to the microwave signal) changing over time.

The magnetic flux $\Phi_{dc} = \Phi_{in} + \Phi_{mod}$ is composed of the preset noise-free input signal, the noise-free flux ramp signal as well as the flux noise time trace derived in the previous step (see section II A). Both, open-loop and FRM readout, can be modeled using the simulation framework, depending on the chosen input parameters. For open-loop readout, the modulation signal takes a predefined constant values representing a static magnetic flux bias. For flux ramp modulation, the flux signal is time-dependent and takes the shape of a sawtooth signal with ramp reset rate f_{ramp} and amplitude $\Phi_{mod}^{max} = M_{mod} I_{mod}^{max}$. Here, I_{mod}^{max} denotes the amplitude of the current running through the modulation coil and M_{mod} the mutual inductance between SQUID and modulation coil. Optionally, a Butterworth lowpass filter with predefined filter order R and cutoff frequency f_{cutoff} can be applied to the flux ramp signal to mimic a real system with finite bandwidth.

C. Step 3: Derivation of the effective inductance shift

Our simulation framework provides three methods to calculate the time-dependent effective change $\Delta L_{T,k}$ of the inductance of the readout resonator as caused by the SQUID. More precisely, it allows to choose between two analytical equations for the limiting cases of either very weak, i.e. negligible probe tone power P_{exc} or very small, i.e. vanishing screening currents in the SQUID loop. The first scenario can be applied for arbitrary values of the screening parameter $\beta_L < 1$ as long as $P_{\text{exc}} \rightarrow 0$, the second method is valid for any value of the probe tone power P_{exc} as long as $\beta_L \ll 1$. However, in most cases and in particular in situations relevant for applications neither of both situations applies. For this reason, our simulation framework provides a third method that takes into account both, finite values of the probe tone power P_{exc} as well as finite values of the screening parameter up to $\beta_L \approx 0.6$. The latter method is based on our most recent microwave SQUID multiplexer model²⁰. For this part of the simulations, the SQUID inductance L_S , the critical current I_c , the geometric coupling parameter k_T between resonator and SQUID as well as the mutual inductance M_{mod} between modulation coil and SQUID are input parameters for the simulation. In addition, the dc flux Φ_{dc} within in the SQUID loop (see section II B) derived in the previous step as well as the magnetic flux contribution Φ_{rf} induced by the current flowing within the resonator enter. It is worth mentioning that for the second and third method, the implicit nature of the underlying equations (see sections III B and III C) requires to use an iterative numerical approach to calculate an accurate prediction of the time-dependent magnetic flux contribution as caused by the microwave currents within the resonator.

D. Step 4: Calculation of the actual resonance frequency

Based on the effective inductance shift ΔL_T , the predefined resonator parameters as well as the generated noise trace due to TLS noise (see section III), the time-dependence of resonance frequency $f_{\text{res},k}$ is calculated. Here, the predefined resonator parameters are the unloaded resonance frequency $f_{\text{res},0}$, the resonator inductance L_R , the coupling inductance L_T , the coupling quality factor Q_c , the loaded quality factor Q_l and the impedance Z_0 of the transmission line. Again, in case that one of both methods taking into account the dependence of the effective inductance shift on the probe tone power (see sections III B and III C) is used, this step has to be performed iteratively as the effective inductance shift ΔL_T depends on the microwave power stored in the resonator which depends on the resonance frequency f_{res} being determined by the effective inductance shift ΔL_T . Once the resonance frequency f_{res} is calculated, the effective resonance frequency noise caused by TLS is added to yield the time trace of the resonance frequency $f_{\text{res},k}$.

E. Step 5: Derivation of the transmission coefficient

The final step of a single simulation run is the calculation of the transmission $S_{21,k}$. Since the modulation of the resonance frequency, especially for FRM readout, can be rather fast, a steady-state approximation for the resonator response is no longer applicable. For this reason, our simulation framework considers the non-equilibrium dynamics of the resonator response to first order. After deriving the complex transmission coefficient $S_{21,k}$, amplifier noise is added. This yields the final output of the simulation which is subsequently processed using the same methods as employed for analyzing measured data.

III. DETAILED DESCRIPTION OF THE SIMULATION FRAMEWORK

The first step when performing a single simulation run is the generation of the noise time traces. The method used to generate noise is identical for all three sources, solely the power spectral density differs. The goal is to synthesize a random discrete time trace x_k of noise at discrete points $t_k = k/f_s$ in time, with $k = 0, \dots, N-1$ and $N \in \mathbb{N}$, with a given noise spectral density of $\hat{S}_x(f)$. Here, f_s is the rate at which the signal is sampled. For this, noise coefficients \hat{a}_j in frequency space are generated with amplitudes

$$|\hat{a}_j| = \begin{cases} \sqrt{\hat{S}_x(f_s \frac{j}{N})} & \text{for } j = -\frac{N}{2}, -\frac{N}{2} + 1, \dots, \frac{N}{2} - 1 \\ 0 & \text{for } j = 0 \end{cases} \quad (1)$$

and random phases θ_j following a uniform distribution

$$\hat{a}_j = |\hat{a}_j| e^{i\theta_j}, \quad \theta_j \in [0, 2\pi). \quad (2)$$

The noise coefficient \hat{a}_0 at zero frequency must vanish to ensure zero-mean noise, regardless of the targeted noise spectral density. Using an inverse fast Fourier transform yields a complex-valued discrete noise time trace:

$$x_k = \sqrt{\frac{f_s}{2}} \sum_{j=-N/2}^{N/2-1} e^{2\pi i \frac{jk}{N}} \hat{a}_j, \quad k = 0, \dots, N-1 \quad (3)$$

In case that real-valued noise is needed, the sum of the real and imaginary contributions of each x_k is used. The spectral density of the noise remains the same. In the simulations, the transmission noise caused by the amplifier is complex-valued, whereas the flux noise in the SQUID and the resonance frequency noise are real-valued.

The noise time traces of the various sources are subsequently included into the generation of the transmission data, along with a set of device- and readout parameters as well as a signal time trace defining the input flux into the SQUID loop. The external flux contribution $\varphi_{\text{dc},k} = \varphi_{\text{sig},k} + \varphi_{\text{mod},k} + \delta\varphi_k$ (from here on we use normalized magnetic flux values, i.e. $\varphi \equiv 2\pi\Phi/\Phi_0$) is the sum of the flux signal time trace $\varphi_{\text{sig},k}$, the modulation flux $\varphi_{\text{mod},k}$ and the magnetic flux noise $\delta\varphi_k$. Each of these contributions are assumed to be sufficiently slow

to be considered quasi-static with respect to the resonance frequency f_{res} .

In a microwave SQUID multiplexer operated with flux ramp modulation for output signal linearization, a sawtooth-shaped modulation current I_{mod} is applied to the modulation coil, which is inductively coupled to the SQUID. The mutual inductance between SQUID loop and modulation coil is M_{mod} , leading to a modulation flux $\varphi_{\text{mod}} = 2\pi M_{\text{mod}} I_{\text{mod}} / \Phi_0$. In the simulation framework, a modulation current time trace $I_{\text{mod},k}$ is generated, based on a specified ramp repetition rate f_{ramp} and amplitude $I_{\text{mod}}^{\text{max}}$. In software, a sawtooth shape with infinitely steep resets and perfectly linear ramp segments can be generated. However, to be more representative of a real measurement setup, a Butterworth lowpass filter may be applied to the modulation current time trace $I_{\text{mod},k}$ in order imitate filtering effects from real signal generators and transmission lines. If open-loop readout is simulated, the modulation flux takes a value $\varphi_{\text{mod},k} = \varphi_{\text{bias}}$ constant in time. This bias flux is typically chosen such that the flux-to-transmission transfer coefficient $K_{\Phi}(\varphi_{\text{bias}}) = K_{\Phi}^{\text{max}}$ is maximized. Open-loop readout is linear only for small signal flux values significantly smaller than a single flux quantum Φ_0 .

The exact process to derive the resonance frequency time trace $f_{\text{res},k}$ depends on the specific assumptions we can make about the device, leading to different expressions for the inductance shift ΔL_T . The specific methods will be discussed in the following.

A. Vanishing probe tone power $\Phi_{\text{rf}} \rightarrow 0$

One limiting case for which an analytic solution for the inductance shift ΔL_T exists is the case of vanishing probe tone power, resulting in a vanishing radio frequency flux amplitude $\Phi_{\text{rf}} \rightarrow 0$. In this case, the effective shift in the coupling inductance L_T is given by the expression

$$\Delta L_T = \frac{M_T^2}{L_S} \frac{\beta_L \cos(\varphi_{\text{tot}})}{1 + \beta_L \cos(\varphi_{\text{tot}})}. \quad (4)$$

In order to calculate the inductance shift ΔL_T using this equation, we have to determine the total flux φ_{tot} threading the SQUID loop. Due to screening currents running in the SQUID loop φ_{tot} is given by the implicit expression²⁰

$$\varphi_{\text{tot}} = \varphi_{\text{dc}} - \beta_L \sin(\varphi_{\text{tot}}). \quad (5)$$

Despite being an implicit equation, this relation is unique for $\beta_L < 1$ and can be inverted to the explicit expression

$$\varphi_{\text{dc}} = \varphi_{\text{tot}} + \beta_L \sin(\varphi_{\text{tot}}). \quad (6)$$

This relation is then evaluated at 1000 linearly spaced data points $\varphi_{\text{tot},j} \in [0, 2\pi)$ yielding an equal number of points $\varphi_{\text{dc},j}$. Since the relation is unique, a cubic spline interpolation to the dataset can be performed, yielding an interpolation function $f(\varphi_{\text{dc}})$ such that $f(\varphi_{\text{dc},j}) = \varphi_{\text{tot},j}$. Since the dependence of the inductance shift ΔL_T on the flux φ_{tot} is periodic in 2π , the restriction to nodes $\varphi_{\text{tot},j}$ on the interval $[0, 2\pi)$ is sufficient. Using the interpolation function $f(\varphi_{\text{dc}})$, we calculate the total flux $\varphi_{\text{dc},k}$ for each value of $\varphi_{\text{ext},k}$ for the given time trace which is used in the subsequent evaluation of equation 4 to obtain an inductance shift time trace $\Delta L_{T,k}$. Once the inductance shift has been calculated, the resulting resonance frequency time trace $f_{\text{res},k}$ is derived using the equation

$$f_{\text{res},k} = f_{\text{res},0} \left(1 - \frac{\Delta L_{T,k}}{L_R + L_T} \right)^{-\frac{1}{2}}. \quad (7)$$

B. Vanishing screening currents $\beta_L \rightarrow 0$

In the case of vanishing screening currents within the SQUID loop, there also exists an analytic solution for the inductance shift ΔL_T ²⁰:

$$\Delta L_T = \frac{M_T^2 \beta_L}{L_S} \frac{2J_1(\varphi_{\text{rf}})}{\varphi_{\text{rf}}} \cos(\varphi_{\text{dc}}). \quad (8)$$

Here, the radio frequency flux amplitude φ_{rf} enters. This flux contribution is caused by the microwave current running in the coupling inductance L_T of the resonator, and thus depends on the energy stored within the resonator. This energy in turn depends on the relative position of the resonance frequency f_{res} to the probe tone f_{exc} . Since the resonance frequency itself depends on the inductance shift ΔL_T , an implicit behavior arises, and equation 8 can't be solved directly. The radio frequency flux amplitude is given by $\varphi_{\text{rf}} = 2\pi M_T I_T / \Phi_0$ with the mutual inductance $M_T = k_T \sqrt{L_T L_S}$ between the SQUID loop and the coupling inductor and the amplitude I_T of the microwave current running in the coupling inductor. The latter is calculated using the expression

$$I_T(f_{\text{exc}}) = \sqrt{2P_{\text{exc}} Z_0} \frac{2\pi f_{\text{exc}} \sqrt{\frac{2}{Z_0(2\pi f_{\text{res}})^2 L Q_c}}}{\left(2i - 2\pi f_{\text{exc}} \sqrt{\frac{2}{Z_0(2\pi f_{\text{res}})^2 L Q_c}} Z_0 \right) \left(\frac{f_{\text{exc}}^2}{f_{\text{res}}^2} - 1 \right) + \frac{f_{\text{exc}}^3}{f_{\text{res}}^2} \frac{2}{Q_c}} \quad (9)$$

To derive the resonance frequency time trace $f_{\text{res},k}$, we evaluate Eq. 8 assuming a vanishing radio frequency flux $\varphi_{\text{rf},k}^0 = 0$. For this, we derive a first guess $f_{\text{res},k}^0$ using Eq. 7. We then

use our guess to calculate a more accurate guess $\varphi_{\text{rf},k}^1$ for the amplitude of the radio frequency flux using Eq. 9. Then, these steps are repeated until subsequent results for the resonance

frequency have a sufficiently small deviation:

$$\varphi_{\text{rf},k}^0 = 0 \quad \forall k, \quad (10)$$

$$\hat{f}_{\text{res},k}^m = \widetilde{f}_{\text{res}}(\varphi_{\text{dc},k}, \varphi_{\text{rf},k}^m), \quad (11)$$

$$\varphi_{\text{rf},k}^{m+1} = \widetilde{\varphi}_{\text{rf}}(\hat{f}_{\text{res},k}^m, f_{\text{exc},k}). \quad (12)$$

up until

$$\sum_{k=0}^N \frac{\hat{f}_{\text{res},k}^M - \hat{f}_{\text{res},k}^{M-1}}{\hat{f}_{\text{res},k}^M} \leq \varepsilon_f \quad (13)$$

at some $M \in \mathbb{N}$ for a given maximum tolerable difference ε_f . The result $f_{\text{res},k} \equiv f_{\text{res},k}^M$ is the resonance frequency time trace used for the remaining part of the simulation run. In this description, $\widetilde{f}_{\text{res}}(\varphi_{\text{dc}}, \varphi_{\text{rf}})$ refers to equations 7 and 8, and $\widetilde{\varphi}_{\text{rf}}(f_{\text{res}}, f_{\text{exc}})$ follows from equation 9. By design, this method only works satisfyingly if $\hat{f}_{\text{res},k}^m$ converges for increasing iteration number m . In operation this has been the case for all reasonable choices of simulation parameters tested so far.

C. General case

In general, both the screening parameter β_L and the probe tone power P_{exc} take finite values. For describing the underlying physics, our most recent multiplexer model yields the expression²⁰

$$\Delta L_T = \frac{M_T^2 \beta_L}{L_S} \frac{2}{\varphi_{\text{rf}}} \sum_{i,j} a_{i,j} \beta_L^{b_{i,j}} J_1(c_{i,j} \varphi_{\text{rf}}) \cos(c_{i,j} \varphi_{\text{ext}}) \quad (14)$$

which is valid for $\beta_L \leq 0.6$. Here, $a_{i,j}$, $b_{i,j}$ and $c_{i,j}$ are coefficient that are listed in²⁰. To derive the inductance shift ΔL_T in the general case, the same recursive method as described in section III B is used. The sole difference is that Eq. 14 is used instead of Eq. 8. Once the resonance frequency time trace $\hat{f}_{\text{res},k}$ has been derived, an effective resonance frequency noise $\delta f_{\text{res},k}$ is added, representing the noise contribution of two-level systems affecting the resonance frequency. The resonance frequency including noise $f_{\text{res},k} = \hat{f}_{\text{res},k} + \delta f_{\text{res},k}$ is used in the subsequent calculation of the transmission time trace $\hat{S}_{21,k}$.

Assuming a sufficiently slow modulation of the resonance frequency, the transmission of a resonator can be approximated by the steady-state expression

$$S_{21}^{\text{SS}}(t) \approx \frac{\frac{Q_1}{Q_i} + 2iQ_1 \delta f(t)}{1 + 2iQ_1 \delta f(t)} \quad (15)$$

with the relative frequency difference $\delta f(t) = (f_{\text{exc}} - f_{\text{res}}(t))/f_{\text{res}}(t)$. However, in the typical operation regime of a microwave SQUID multiplexer, the resonance frequency $f_{\text{res}}(t)$ changes swiftly enough that it can not be approximated as quasi-static and a dynamical resonator description has to be used. The dynamical behavior of the transmission parameter S_{21} of a lumped element microwave resonator with a variable inductance can be approximated to first order as follows:

$$S_{21}(t_0 + \Delta t) \approx S_{21}^{\text{SS}}(t_0 + \Delta t) + [S_{21}(t_0) - S_{21}^{\text{SS}}(t_0 + \Delta t)] e^{-\pi \Delta f_{\text{BW}} \Delta t + i(\omega_{\text{res}} - \omega) \Delta t}. \quad (16)$$

If an initial value of $S_{21}(t_0)$ at a time t_0 is known, the transmission parameter $S_{21}(t_0 + \Delta t)$ at a future point in time for a sufficiently small time difference Δt can be derived. Applying this method over and over again allows us to generate a time trace of arbitrary length. It is worth mentioning that this approximation only holds if we can assume S_{21}^{SS} to be quasi-static on the time scale Δt . In the simulation, we use the steady state value $\hat{S}_{21,0} = S_{21}^{\text{SS}}(t_0)$ for the initial time t_0 as starting value. The time interval $\Delta t = t_{k+1} - t_k = 1/f_s$ is given by the sampling rate f_s :

$$\hat{S}_{21,0} = \hat{S}_{21,0}^{\text{SS}}, \quad (17)$$

$$\hat{S}_{21,k+1} = \hat{S}_{21,k+1}^{\text{SS}} + (\hat{S}_{21,k} - \hat{S}_{21,k}^{\text{SS}}) e^{-\pi[\Delta f_{\text{BW}} + 2i(f_{\text{res},k} - f_{\text{exc},k})] \Delta t}. \quad (18)$$

Finally, transmission noise $\delta S_{21,k}$ is added, representing amplifier noise caused by the HEMT amplifier, yielding the final simulation result:

$$S_{21,k} = \hat{S}_{21,k} + \delta S_{21,k}. \quad (19)$$

The relation between the transmission noise spectral density \hat{S}_{S21} and the system noise temperature T_N is given by:

$$\sqrt{\hat{S}_{S21}} = 2 \sqrt{\frac{2k_B T_N}{P_{\text{exc}}}}. \quad (20)$$

This simulated transmission time trace resembles a measurement on a μ MUX device with the given parameters and can be evaluated by the same methods used for analysing experimental data. If flux ramp modulation is used, demodulation of the transmission time trace yields the output signal flux $\varphi_{\text{out},j}$:

$$\varphi_{\text{out},j} = \arctan \left[\frac{\sum_{k=jW}^{(j+1)W-1} \sin(2\pi j f_{\text{mod}}/f_{\text{res}}) |S_{21,k}|}{\sum_{k=jW}^{(j+1)W-1} \cos(2\pi j f_{\text{mod}}/f_{\text{res}}) |S_{21,k}|} \right], \quad (21)$$

with the modulation frequency $f_{\text{mod}} = f_{\text{ramp}} M_{\text{mod}}^{\text{max}}$ and the number $W = f_s/f_{\text{ramp}}$ of data points in between resets of the modulation ramp. Naturally, the resulting signal time trace $\varphi_{\text{out},j}$ has a factor of W fewer points than the transmission time trace $S_{21,k}$ computed previously. If open-loop readout is used, the signal flux time trace $\varphi_{\text{out},k}$ can be calculated from the transmission time trace $S_{21,k}$ using the transfer coefficient $K_{\Phi}(\varphi_{\text{bias}})$:

$$\varphi_{\text{out},k} = \frac{S_{21,k}}{K_{\Phi}(\varphi_{\text{bias}})}. \quad (22)$$

Here, the transfer coefficient $K_{\Phi}(\varphi_{\text{bias}})$ is determined during the simulation by numerically calculating the transmission-to-flux characteristic $S_{21}(\varphi_l)$ for 1024 linearly spaced data points of $\varphi_l \in [0, 2\pi)$, and then subsequently calculating the numerical derivative at the specified bias flux value φ_{bias} . The signal flux time trace has the same number of data points as the transmission time trace $S_{21,k}$.

If a noise analysis needs to be performed, e.g. to calculate a noise spectral density, a modified Welch's method²¹ is applied to the output signal flux time trace. This method is based

on the calculation of a number of Q individual periodograms $P^q(f)$, each of which covers a subset of data points of the output signal time trace $\varphi_{\text{out},k}$. The length of these subsets L must be smaller than the total number of data points in the output signal time trace $\varphi_{\text{out},k}$, and subsequent subsets overlap with $L - D$ datapoints. All Q datasets combined cover the entire data set of $\varphi_{\text{out},k}$. Each periodogram is then given by

$$P^q(f) = \frac{2}{f_s \sum_{n=0}^{L-1} w_n^2} \left| \sum_{n=0}^{L-1} w_n \varphi_{\text{out},qD+n} e^{-2\pi i f n / f_s} \right|^2, \quad (23)$$

with the weights w_n of a window function. For the data presented in this paper, a Blackman-Harris window was used. The estimator $S_\Phi(f)$ of the noise spectral density of the output signal time trace $\varphi_{\text{out},k}$ is then given by the average of all periodograms:

$$S_\Phi(f) = \frac{1}{Q} \sum_{q=0}^{Q-1} P^q(f). \quad (24)$$

If the length L of the subsets is chosen large, then the estimator $S_\Phi(f)$ contains information even down to low frequencies f . However, the number Q of individual sets is rather small, and only few individual periodograms can be averaged, leading to a low fidelity of the estimator. A choice of short window lengths L results in many subsets and thus a high fidelity of the estimator, but the estimator can not resolve low frequencies. In this paper, we hence repeat this process for multiple different window lengths L_i . The combination of different subset lengths allows both a high estimator fidelity at large frequencies f as well as information about low frequencies, albeit at a lower fidelity.

IV. DEFAULT SIMULATION PARAMETERS

Our simulation framework can be used for simulating the characteristics and performance of microwave SQUID multiplexers with virtually arbitrary input parameters. We presently apply/recommend only a weak boundary condition, i.e. the input parameters should fall within the range for which our model of the microwave SQUID multiplexer has been approved, i.e. $\beta_L \leq 0.6$, $Q_i > 1000$ and, $4 \text{ GHz} \leq f_{\text{res},0} \leq 8 \text{ GHz}$ ²⁰. We presently investigate whether our model is still valid for higher resonance frequencies and work on model expansions to describe adequately the multiplexer behavior for hysteresis parameters $\beta_L \rightarrow 1$.

In subsequent sections, we present some sanity checks and compare simulation to experimental data to proof the reliability of our simulation framework and discuss predictions of our simulation framework aiming towards a full multiplexer optimizations. As the number of input parameters is somehow gigantic (see figure 2) resulting in the necessity to run an enormously large number of simulations to find an optimized set of parameters, we start with varying only a small number of all free simulation parameters at once and postpone the discussing of a full multiplexer characterization to a later publication. The default set of simulation parameters

is based on our recent activities regarding the development of a microwave SQUID multiplexer for the ECHO experiment²² which aims to investigate the electron neutrino mass with sub-eV/ c^2 sensitivity.

The latest generation of ECHO multiplexers employs lumped element microresonators that are formed by a meander-shaped inductor with inductance $L_R = 2 \text{ nH}$, a load inductor with inductance $L_T = 152 \text{ pH}$ and an interdigital capacitor whose capacitance C is set to yield a unique unloaded resonance frequency $f_{\text{res},0}$ in the frequency band from 4 GHz to 8 GHz. For our simulation, we set $f_{\text{res},0} = 6 \text{ GHz}$ if not otherwise noted. We typically assume an internal quality factor of $Q_i = 1 \times 10^5$ and adjust the effective coupling capacitance C_C^{eff} (which includes both the coupling inductance C_C and the parasitic inductance C_{para} as described in section I) to yield a bandwidth of $\Delta f_{\text{BW}} = 1 \text{ MHz}$. Moreover, we set the SQUID loop inductance to $L_S \simeq 46 \text{ pH}$ and adjust the critical current I_c of the Josephson tunnel junction to yield a hysteresis $\beta_L = 0.4$, unless noted otherwise. The mutual inductance M_T is usually chosen to yield $\Delta f_{\text{res}}^{\text{max}} = \Delta f_{\text{BW}}$ and tuned by changing the value of the coupling factor k_T . It is worth noting that the Bessel function of the first kind, which appears in equation 14 can lead to jumps in the SQUID response if the radio frequency flux amplitude becomes too large. To mitigate this effect, for the assumed internal quality factor Q_i in this publication the value of the coupling factor k_T has been restricted such that the resonance frequency shift does not exceed 5 times the resonator bandwidth $\Delta f_{\text{res}}^{\text{max}} \leq 5 \Delta f_{\text{BW}} = 5 \text{ MHz}$. The sampling rate of the artificial data acquisition system $f_s = 15.625 \text{ MHz}$ corresponds to the effective sampling rate of the DAQ system presently developed for the ECHO experiment^{23,24}.

For flux ramp modulation, we select a default ramp height of $1 \Phi_0$ at a ramp reset rate of $f_{\text{ramp}} = f_s / 128 \approx 122.1 \text{ kHz}$ with infinitely steep edges at reset. This rate is low enough to exclude noise increasing effects due to the finite resonator response time. Additionally, this yields ramp segments with $2^7 = 128$ data points each such that our FFT algorithms works without zero padding. An excitation frequency $f_{\text{exc}} = f_{\text{res},0} + 0.3 \text{ MHz}$ is assumed, which is slightly above the largest flux-dependent resonance frequency f_{res} reached during modulation. Finally, we consider in most cases only amplifier noise with an amplifier chain input noise temperature of $T_N = 4 \text{ K}$ as resulting from state-of-the-art HEMT amplifiers connected to the multiplexer via superconducting coaxial cables and a cryogenic isolator. Finally, it is worth to mention that we performed all simulations presented with the general multiplexer model, i.e. $\beta_L > 0$, $\varphi_{\text{rf}} > 0$, as described in section III C. The resulting values of the device- and readout parameters are depicted in figure 3. For clarity, some parameters with a default value of zero, such as TES noise, SQUID noise and low-pass filter parameters for the modulation ramp have been omitted.

V. VALIDATION OF THE SIMULATION FRAMEWORK

In order to verify correct functioning of our simulation framework, we performed several sanity checks. We individ-

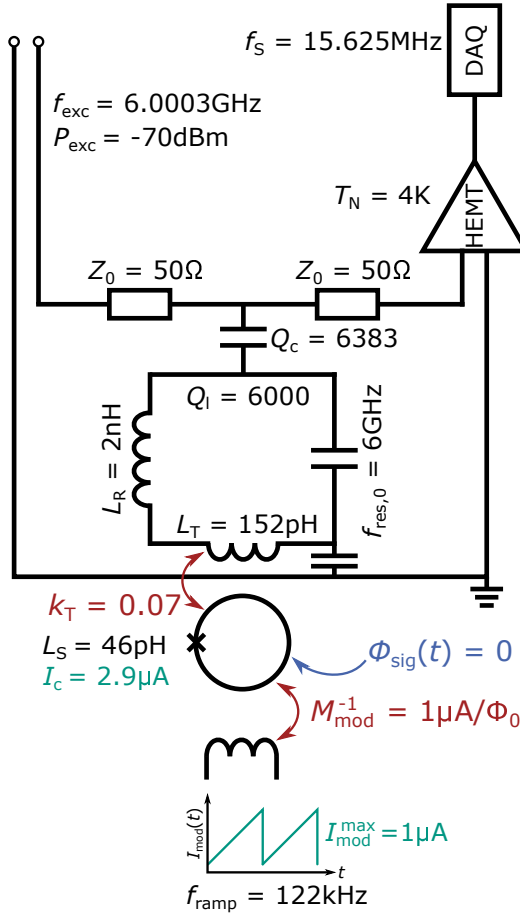


FIG. 3. Schematic circuit diagram of a single readout channel as considered during numerical simulation. Non-zero default values of device- and readout parameters are depicted. The individual symbols are explained in the main text. The odd value of the coupling quality factor Q_c was chosen to yield a loaded quality factor $Q_l = 6000$ at an internal quality factor of $Q_i = 1 \times 10^5$. Zero value parameters such as noise sources not used by default are omitted for clarity.

ually tested all functions and simulation steps within a single simulation run such as noise generation, flux ramp modulation and demodulation as well as the calculation of the transmission coefficient $S_{21,k}(t)$ and proofed that our simulation reflects simple expectations. This includes, for example, the scaling of the white noise level of the simulated overall noise spectral density with the system noise temperature. Moreover, we comprehensively compared simulation results to experimental data and proofed consistency among related data sets. While most of these sanity checks are quite 'simple' and hence not appropriate to be discussed within a paper, we want to discuss two more advanced sanity checks as they not only proof the correct functioning of our simulation framework but also that our software is able to describe experimental data that is hard to describe otherwise.

A. Dependence of the flux noise on the probe tone power

The evaluation of the noise performance of a microwave SQUID multiplexer for a given set of device and readout parameters is one of the core applications of our simulation framework. As such, a comparison between experimental data and simulation results of the dependence of the square root of the white magnetic flux noise density $\sqrt{S_{\Phi, \text{white}}}$ on probe tone power P_{exc} provides a reasonable sanity check. To make such a comparison, we comprehensively characterized one of our most recent microwave SQUID multiplexers based on lumped element microresonators and compared the acquired data to simulation results. Figure 4 shows both, measured data and simulation results, of a example multiplexer channel having an unloaded resonance frequency of $f_{\text{res},0} = 4.86$ GHz, while the resonator bandwidth Δf_{BW} , maximum resonance frequency shift $\Delta f_{\text{res}}^{\text{max}}$, internal quality factor Q_i and screening parameter β_L take values of $\Delta f_{\text{BW}} = 3.1$ MHz, $\Delta f_{\text{res}}^{\text{max}} = 0.95$ MHz, $Q_i = 6400$ and $\beta_L = 0.4$, respectively. The measurement was performed with open-loop readout at a fixed magnetic bias flux $\Phi_{\text{bias}} \approx 0.25 \Phi_0$. Using the measured or predefined multiplexer and readout parameters, we afterwards simulated the expected dependence $\sqrt{S_{\Phi, \text{white}}}(P_{\text{exc}})$ using our simulation framework. The only free parameter in the simulation was the effective system noise temperature T_N which we haven't determined experimentally. The agreement between experimental data and simulation results is quite impressive in particular close to and below the minimum where the multiplexer would be operated in a real application. The only slight deviation is close to the peak around -60 dBm and results from the measurement uncertainty of the multiplexer transfer coefficient which gets very small close to the peaks in the flux noise spectral density (we refer the interested reader to²⁰ for a detailed discussion of the reason of the peak occurrence). Overall, this nicely proves that our simulation framework is able to resemble the characteristics and performance of real multiplexer devices.

It is worth mentioning that one might be inclined to describe the dependence of the measured white noise level on probe tone power directly using the expression as given by our most recent multiplexer²⁰. In this case, we expect that the experimental data should follow the dependence $\sqrt{S_{\Phi, \text{white}}(\Phi_{\text{rf}})} \propto J_1^{-1}(\Phi_{\text{rf}})$ (compare figure 4). For low values of the excitation power P_{exc} , the dependence should follow the intuitive expectation $\sqrt{S_{\Phi, \text{white}}} \propto 1/\sqrt{P_{\text{exc}}}$. However, as the probe tone power P_{exc} and thus the rf magnetic flux Φ_{rf} within the SQUID loop increases, the amplitude of the SQUID response is expected to decrease²⁰. This leads to a degradation of the signal-to-noise ratio in the transmission $S_{21}(t)$ and thus to an increase of noise after flux ramp demodulation. Ultimately, this results firstly in a distinct global minimum, the position and depth of which depend on the device parameters, and secondly in an oscillatory behavior for large probe tone powers. Here, the dependence of the SQUID response on probe tone power dominates the behavior of the flux noise, and wherever the SQUID response amplitude vanishes, a sharp peak in the readout flux noise occurs.

While this simple expectation gives a rough estimate for

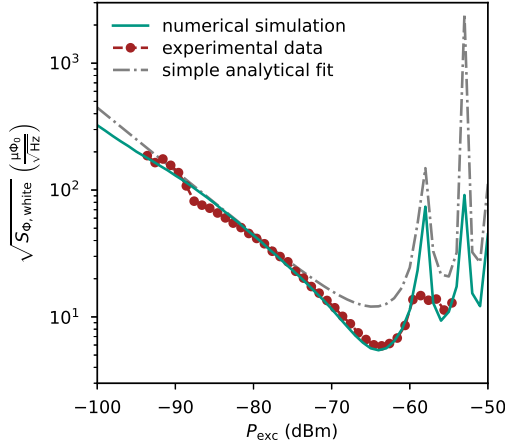


FIG. 4. Measured dependence of the white magnetic flux noise level $\sqrt{S_{\Phi, \text{white}}}$ on the probe tone power P_{exc} . The data were acquired for an example channel of our most recent microwave SQUID multiplexer with lumped-element microresonators. Details about the device and readout parameters are given in the main text. The measurement was done in open-loop mode, i.e. without flux ramp modulation. In addition to measured data, the expected dependence using a simple analytical approach as well as simulation results as obtained with our simulation framework are shown.

the dependence of the white noise level of the square root of the magnetic flux noise spectral density $\sqrt{S_{\Phi, \text{white}}}$ on the probe tone power P_{exc} , it can clearly be seen that the shape of the minimum is not described well. One the other hand, the simulated data models the experimental results much more closely, especially around the minimum. For the experimental data, the region for low readout powers is slightly convex rather than strictly linear as in the analytical description, leading to a lower minimum of a slightly different shape. Since the SQUID response for finite screening currents is no longer sinusoidal, the optimal value magnetic bias flux $\Phi_{\text{bias}}^{\text{opt}}$ depends on the probe tone power P_{exc} . If a constant value Φ_{bias} of the bias flux is used, as done in the measurement depicted here, this leads to an additional factor influencing the total readout flux noise. While a simple analytical model does not include this contribution, it is described with excellent agreement by the simulations.

B. Bandwidth- and noise penalty of hybrid microwave SQUID multiplexing

Flux ramp modulation based hybrid SQUID multiplexing is a very recent multiplexing scheme that allows for reducing the number of readout resonators within a microwave SQUID multiplexer while keeping the number of readout channel constant¹⁸. It might revolutionize SQUID based multiplexing of large-scale bolometric cryogenic detector arrays as fabrication accuracy is presently setting strong constraints on the number of readout channels there. A hybrid SQUID multiplexer ($H\mu$ MUX) closely resembles a regular μ MUX, with the major difference that multiple (instead of a single) rf-

SQUIDs, each being equipped with an individual input coil and coupled with different strength to the FRM modulation coil, are coupled to the termination inductance L_T of a readout resonator. During flux ramp modulation, each rf-SQUID experiences a different modulation frequency, transducing the different input signals into unique sidebands of the microwave carrier signal probing the readout resonator. In the subsequent two-step demodulation process, the individual input signals are reconstructed. Because of the strong similarity between both SQUID multiplexer types, our simulation software can also be applied to investigate the properties and characteristics of such an advanced hybrid microwave SQUID multiplexer.

As another sanity check of our simulation framework, we tried to resemble the intrinsic bandwidth- and noise penalty of such a hybrid microwave SQUID multiplexer. For this, we performed several simulation runs to determine the dependence of the white noise level of the overall flux noise spectral density $\sqrt{S_{\Phi, \text{white}}}$ on the flux ramp reset rate f_{ramp} for six different $H\mu$ MUX devices differing only by the number N of SQUIDs coupled to the resonator as well as their resonator bandwidth Δf_{BW} . Bandwidth and probe tone power scale linearly with the SQUID number, i.e. $\Delta f_{\text{BW}, N} \propto N$ and $P_{\text{exc}, N} \propto N$ respectively. For $N = 1$, i.e. a conventional microwave SQUID multiplexer, the default values $\Delta f_{\text{BW}, 1} = 1$ MHz and $P_{\text{exc}, 1} = -70$ dBm were assumed. Figure 5(a) shows as an example the simulation results for $N = 1$ and $N = 3$. It clearly shows that at slow flux ramp reset rates $f_{\text{ramp}} \ll 1$ MHz the white flux noise level $\sqrt{S_{\Phi, \text{white}}}$ has a constant base value $\sqrt{S_{\Phi, \text{white}}^{\text{base}}}$. However, as the ramp reset rate increases, the flux noise level starts increasing above some limit frequency $f_{\text{ramp}}^{\text{lim}}$ as the resonator can no longer follow the SQUID modulation due to its finite response time. The limit frequency $f_{\text{ramp}}^{\text{lim}}$ takes different values for each SQUID because of the different mutual coupling between SQUID loop and modulation coil the resulting variation of modulation frequencies. The maximum flux ramp reset rate suitable for operating the device is ultimately limited by the SQUID with the lowest limit frequency. For determining this frequency, we fitted each curve by the empirical function

$$\sqrt{S_{\Phi, \text{white}}(f)} = \sqrt{S_{\Phi, \text{white}}^{\text{base}}} \sqrt{1 + \left(\frac{f}{f_{\text{ramp}}^{\text{lim}}}\right)^b}, \quad (25)$$

(see figure 5). Considering basic information theory, two relations for $H\mu$ MUX with a constant number of total readout channels and constant total readout power can be concluded¹⁸. The maximum usable flux ramp reset rate $f_{\text{ramp}}^{\text{max}} = \min(f_{\text{ramp}, i}^{\text{lim}})$ (determining the lowest limit frequency of all SQUIDs) as well as the white noise level of each readout channel can be described by

$$f_{\text{ramp}}^{\text{max}} \propto \frac{N}{(2N - 1)} \quad (26)$$

and

$$\sqrt{S_{\Phi, \text{white}}} \propto \sqrt{N}. \quad (27)$$

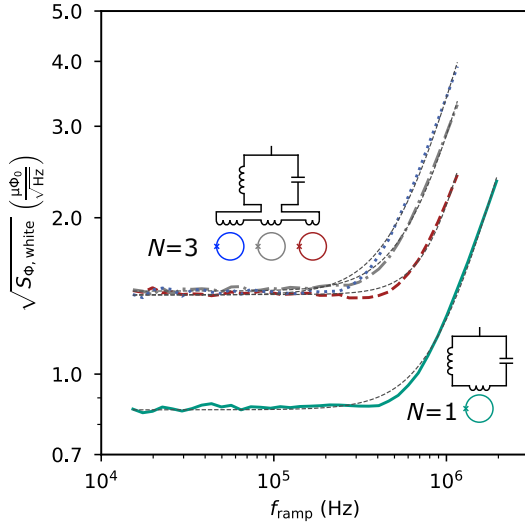


FIG. 5. Dependence of the white magnetic flux noise level $\sqrt{S_{\Phi,\text{white}}}$ on the flux ramp reset rate for a hybrid microwave SQUID multiplexer with $N = 1$ and $N = 3$. The inset shows the respective $H\mu$ MUX configuration where the colors correspond to each other. For further analysis, an empirical function was fitted to each curve (dotted line, see main text).

Figures 6(a) and (b) show the limit frequency white $f_{\text{ramp}}^{\text{lim}}$ as well as white noise level $\sqrt{S_{\Phi,\text{white}}^{\text{base}}}$ as extracted from our simulations and as predicted by basic information theory. The agreement is excellent and proves that our simulation framework can even describe more complicated multiplexer devices.

VI. FIRST STEP TOWARDS FULL μ MUX OPTIMIZATION

Our simulation framework allows determining the white noise level $\sqrt{S_{\Phi,\text{white}}}$ of a single readout channel of a microwave SQUID multiplexer for a predefined set of device and readout parameters within a couple of minutes. This allows finding a parameter configuration which minimizes the overall noise level by systematically varying different parameters. Ideally, the entire configuration space is varied within a set of multiple simulation runs to find a fully optimized device. However, the complexity and hence computational time is exponentially increasing with the number of varied parameters. For this reason and as the full optimization of a microwave SQUID multiplexer is not within the scope of this paper, we restricted the parameter space to a small subset and discuss as an example the optimization of readout noise on (i) the screening parameter β_L , (ii) probe tone frequency f_{exc} , (iii) the readout flux Φ_{rf} probing the rf-SQUID, and (iv) the value for the ratio η between the maximum frequency shift $\Delta f_{\text{res}}^{\text{max}}$ and the resonator bandwidth Δf_{BW} .

A. Dependence of readout noise on screening parameter β_L and probe tone frequency f_{exc}

We run a dedicated set of simulations to determine the dependence of the white noise level $\sqrt{S_{\Phi,\text{white}}}$ on the probe tone frequency f_{exc} for several values of the screening parameter β_L . For each simulation, the mutual inductance M_T between SQUID and resonator was refined to guarantee $\Delta f_{\text{res}}^{\text{max}} = \Delta f_{\text{BW}} 1 \text{ MHz}$. The corresponding results are depicted in figure 7(a). If the probe tone frequency f_{exc} is very close to the unaltered resonance frequency $f_{\text{res},0}$, i.e. $f_{\text{exc}} - f_{\text{res},0} \approx 0$, the actual resonance frequency switches from being below to being above f_{exc} during flux ramp modulation. In this scenario, the shape of the resulting transmission response is non-sinusoidal, compromising FRM demodulation and resulting in enhanced readout noise. This manifests as the central peak in the figure. To either side of the central peak, a local minimum is found. The asymmetry of the curves is related to the asymmetry of the SQUID response due to the non-linear junction equations²⁰.

In figure 7(b), we show the white noise values of both minima for $f_{\text{exc}} > f_{\text{res},0}$ and $f_{\text{exc}} < f_{\text{res},0}$, respectively, for several values of the SQUID hysteresis parameter β_L . It is obvious that for any choice of the screening parameter β_L , choosing $f_{\text{exc}} > f_{\text{res},0}$ yields a lower overall white noise level. This agrees well with our expectation regarding the dependence of both, the resonator transmission spectrum and the SQUID response, on the external magnetic flux. For finite values of the hysteresis parameter β_L , the latter is non-sinusoidal and is further distorted when transduced to a transmission response by the resonator. With $f_{\text{exc}} > f_{\text{res},0}$, the resulting transmission response is closer to a sinusoidal shape, thus leading to a more efficient demodulation and lower readout noise. The broad minimum for $0.3 < \beta_L < 0.5$ shows that for a given parameter set the noise level does not strongly depend on β_L . Assuming the mutual inductance M_T can be tuned in a post fabrication process to yield $\Delta f_{\text{res}}^{\text{max}} = \Delta f_{\text{BW}}$, this significantly relaxes junction fabrication as I_c can easily vary due to fabrication inaccuracies. In figure 8(a) (red), the probe tone frequency yielding the lowest overall noise performance is shown as a function of the hysteresis parameter β_L . It nicely shows that the optimal excitation frequency $f_{\text{exc}}^{\text{opt}}$ can be determined for any set of device parameters.

B. Optimal value of rf flux amplitude Φ_{rf} within the SQUID loop

A critical parameter for μ MUX operation is the rf magnetic flux amplitude Φ_{rf} used for probing/exciting the SQUID. It is set by the probe tone power as well as several design parameters such as the SQUID hysteresis parameter β_L and strongly affects the system white noise level for amplifier limited setups. To investigate the complex interplay between the associated device and readout parameters, the dependence of the white readout flux noise $\sqrt{S_{\Phi,\text{white}}}$ on the probe tone power P_{exc} was simulated for different values of the screening parameter β_L . The mutual inductance M_T was adjusted such that

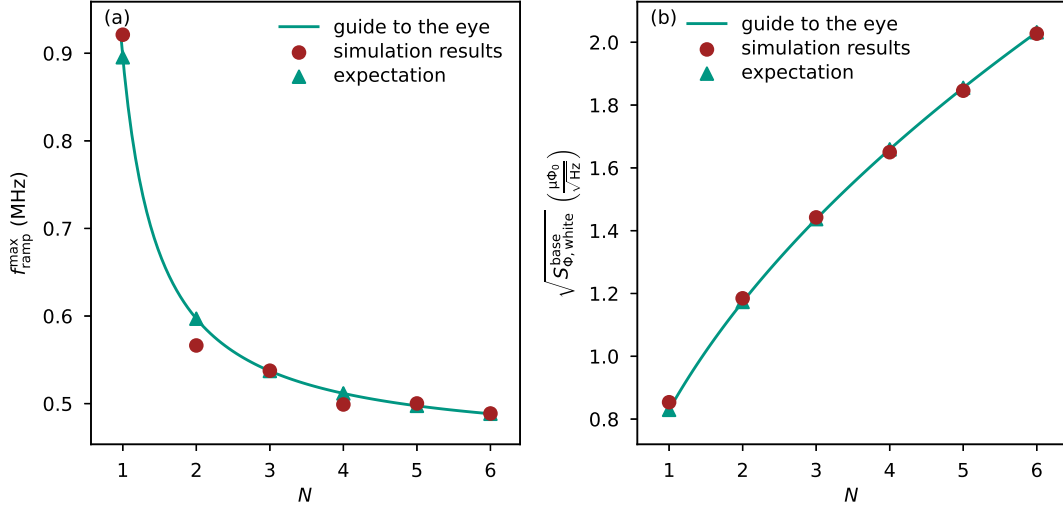


FIG. 6. (a) Limit frequency $f_{\text{ramp}}^{\text{max}}$ of a $H\mu\text{MUX}$ device in dependence on the SQUID number N as extracted from our simulations and as predicted from basic information theory. The SQUID with the lowest limit frequency $f_{\text{ramp}}^{\text{lim}}$ limits the channel bandwidth and has been depicted. A guide to the eye for non-integer N is provided as well. (b) Average white noise level $\sqrt{S_{\Phi,\text{white}}^{\text{base}}}$ in the low frequency limit for each simulated device, as well as predicted from information theory.

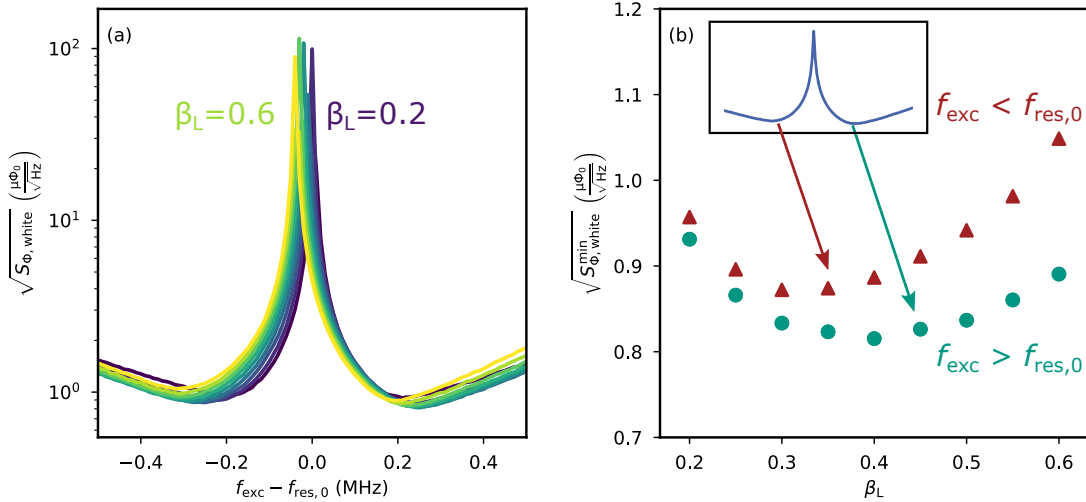


FIG. 7. (a) Dependence of the white readout flux noise $\sqrt{S_{\Phi,\text{white}}}$ on the probe tone frequency f_{exc} for different values of the SQUID hysteresis parameter β_L that was altered by varying the critical current I_c . (b) White noise level $\sqrt{S_{\Phi,\text{white}}^{\text{min}}}$ in both local minima of figure (a) for each value of β_L .

$$\Delta f_{\text{res}}^{\text{max}} = \Delta f_{\text{BW}} = 1 \text{ MHz.}$$

Figure 8(b) shows as an example two acquired simulation curves. The overall shape of the resulting curves was already discussed in section V A. At low excitation powers P_{exc} , the dependence of the white readout flux noise $\sqrt{S_{\Phi,\text{white}}}$ on the probe tone power results from the increasing signal-to-noise ratio, yielding a linear decrease of noise level. At high excitation powers P_{exc} , the power dependence of the SQUID response dominates, resulting in an oscillatory behavior. In between, a distinct global minimum forms, the position and depth of which depend on the value of the screening parameter β_L .

ter β_L .

In figure 8(a), we show the dependence of the radio frequency magnetic flux amplitude $\Phi_{\text{rf}}^{\text{opt}}$ at the probe tone power which minimizes readout flux noise on the screening parameter β_L . It is apparent that $\Phi_{\text{rf}}^{\text{opt}}$ is independent of β_L and that the ideal value is $\Phi_{\text{rf}}^{\text{opt}} \approx 0.30\Phi_0$. Similar results are obtained for other resonance frequencies $f_{\text{res},0}$ indicating a universal behavior. This observation is in good agreement with results reported in²⁵.

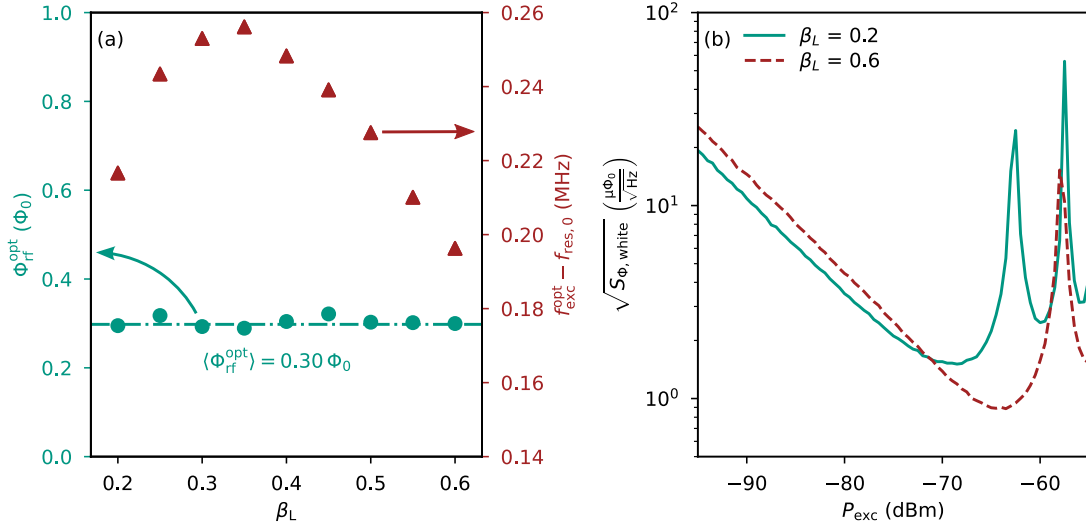


FIG. 8. (a) Dependence of the optimum rf magnetic flux amplitude Φ_{rf}^{opt} yielding the lowest noise floor (\circ , left y-axis) and optimum probe tone frequency f_{exc}^{opt} (∇ , right y-axis) on the SQUID hysteresis parameter β_L . (b) Dependence of the white readout flux noise $\sqrt{S_{\Phi,white}}$ on probe tone power P_{exc} for two different values of β_L .

C. Optimal ratio between maximum frequency shift and the resonator bandwidth

The ratio $\eta = \Delta f_{res}^{max} / \Delta f_{BW}$ between the maximum frequency shift Δf_{res}^{max} and the resonator bandwidth Δf_{BW} is usually chosen close to unity, i.e. $\eta \approx 1$, to guarantee optimal readout conditions^{13,25}. However, this rule of thumb does not take into account that Δf_{res}^{max} , and hence the ratio η , depend both on the probe tone power used for resonator readout, i.e. $\Delta f_{res}^{max} = \Delta f_{res}^{max}(P_{exc})$ and $\eta = \eta(P_{exc})$. Since the maximum frequency shift and the overall white noise floor both depend on the probe tone power, we have to expect a severe deviation from the empirical value $\eta \approx 1$. For this reason, we investigated the effect $\eta_{eff}(P_{exc}) = \Delta f_{res}^{max}(P_{exc}) / \Delta f_{BW}$ on the readout noise. For this, we performed a set of simulations for which we systematically varied the probe tone power P_{exc} for various values of the low-power value $\eta_0 = \lim_{P_{exc} \rightarrow 0} \eta_{eff}(P_{exc})$. Figure 9 summarizes the results of these simulations. Figure 9(a) nicely shows that the position of the noise minimum shifts towards lower readout power as η_0 increases due to the related increase in coupling mutual inductance M_T . For low probe tone powers, the choice of $\eta_0 \approx 1$ leads to the best overall noise level. Moreover, figure 9(b) shows the dependence of noise in the minimum $S_{\Phi,white}^{min}$ on the ratio η_0 . It is obvious that with increasing power, $\eta_0 > 1$ turns out to ultimately yield lower noise as compared to the empirical value $\eta_0 \approx 1$. As the resonance frequency modulation amplitude Δf_{res}^{max} decreases with increasing readout power, so does $\eta_{eff}(P_{exc})$. A proper choice of η_0 leads to the ideal value of $\eta_{eff}(P_{exc}^{opt}) \approx 1$ at the ideal probe tone power rather than in the low power limit, ultimately decreasing readout noise and reducing P_{exc}^{opt} . The latter is an important result taking into account that present multiplexers somehow suffer from intermodulation products related to the IIP3 points of the subsequent amplifier chain²⁶. Hence, reaching the optimum noise level at lower readout

power allows to increase the multiplexing factor for a given amplifier chain.

VII. POTENTIAL OTHER APPLICATIONS OF THE SIMULATION FRAMEWORK

The main application of the simulation framework presented within this paper is the analysis and optimization of the characteristics and performance of a microwave SQUID multiplexer and associated readout devices. However, it can in addition be used to study a variety of effects related to μ MUX operation, two of which we will showcase in this section.

A. Linearity of microwave SQUID multiplexers

Because of the periodicity of the SQUID response, the output signal of a μ MUX has to be linearized if the device is intended to read out detectors with an expected signal amplitude on the order of (or even exceeding) a single flux quantum Φ_0 . This is typically achieved using flux ramp modulation¹⁹. However, the complex interplay between the nonlinear characteristics of a microwave SQUID multiplexer and flux ramp modulation make the analysis of output signal linearity in μ MUX based readout systems by analytical means unfeasible. Second-order effects such as the finite reset time of the flux ramp and the finite resonator response time adds even more complexity. However, our simulation framework allows predicting / investigating device linearity in just a few minutes.

Figure 10(a) shows as an example the dependence of the output signal flux Φ_{out} on the input signal flux Φ_{in} for three microwave SQUID multiplexers with different values of the screening parameter β_L . From a bird's eye view, the rela-

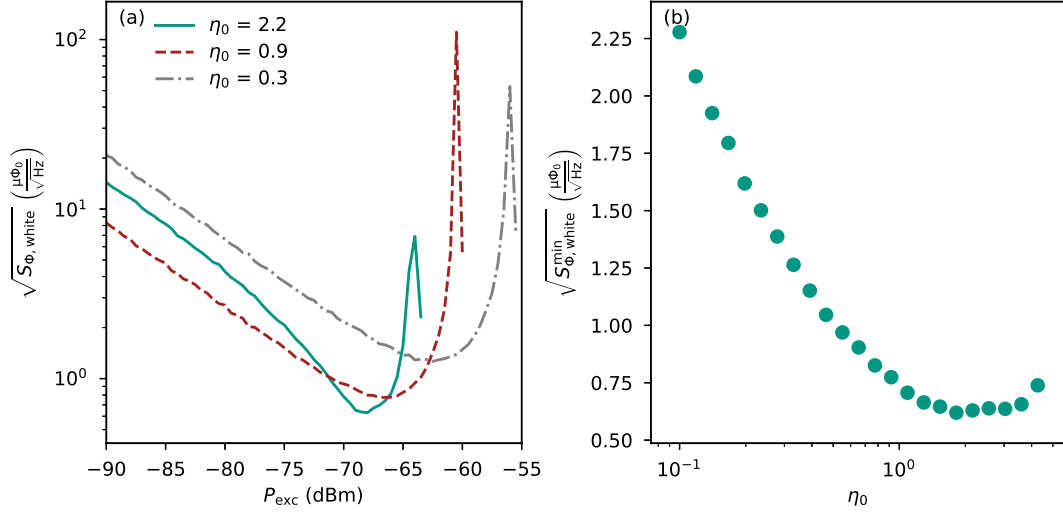


FIG. 9. (a) Dependence of the white noise level $\sqrt{S_{\Phi, \text{white}}}$ of magnetic flux on the microwave probe tone power P_{exc} for three values of η_0 , set by changing the coupling mutual inductance M_T . (b) Dependence of the minimum noise value $\sqrt{S_{\Phi, \text{white}}^{\text{min}}}$ on the ratio parameter $\eta_0 = \lim_{P_{\text{exc}} \rightarrow 0} \eta_{\text{eff}}(P_{\text{exc}})$.

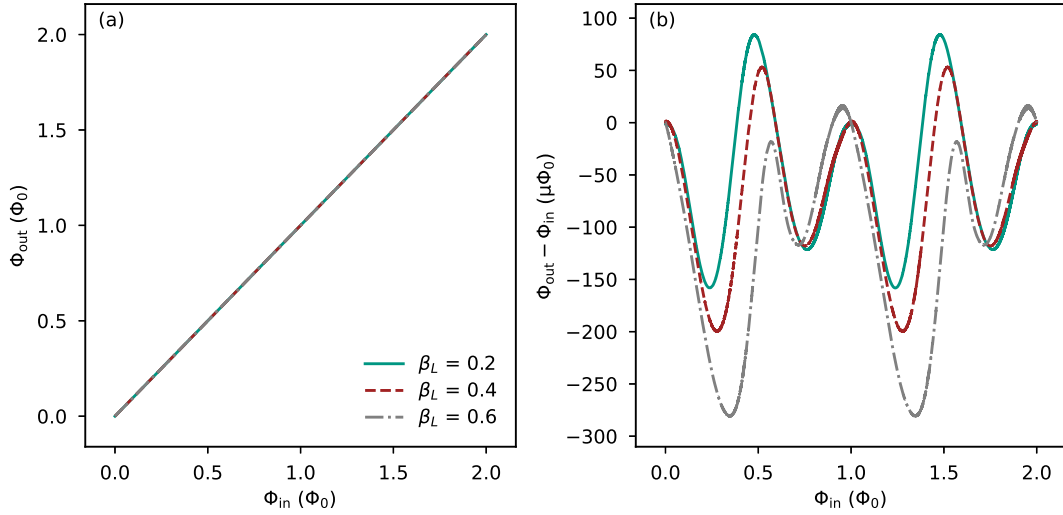


FIG. 10. (a) Output signal flux Φ_{out} in dependence of input signal flux Φ_{in} for different values of the screening parameter β_L . (b) Deviation from perfect linearity, i.e. the difference $\Phi_{\text{out}} - \Phi_{\text{in}}$ in dependence of input signal flux Φ_{in} .

tion between input and output signal looks almost ideally linear. However, subtracting a linear fit from the simulated input-output relation reveals a remaining non-linearity which is shown in figure 10(b). For these simulations, a flux ramp with an amplitude of at most $2.5\Phi_0$ in the SQUID loop was assumed. A second-order Butterworth low-pass filter with a cutoff frequency of $f_{\text{cutoff}} = 10\text{MHz}$ was applied to emulate a finite flux ramp reset time. Datapoints amounting to 20% of each ramp segment were neglected to avoid transients of the ramp resets to affect the demodulation procedure. We didn't add noise traces to focus on systematic nonlinearity only.

Since the FRM method is based on the phase determination of a periodic signal, its non-linearity also has to be pe-

riodic with the same period length of one flux quantum Φ_0 . This behavior is clearly apparent from figure 10(b). The peak to peak range of the non-linearity is roughly $250\mu\Phi_0$ for all three simulated devices. While the value of the screening parameter changes the shape of both the SQUID response and the non-linearity curve, it has very little effect on the magnitude of the deviation from the desired linear behavior for the parameter set assumed here.

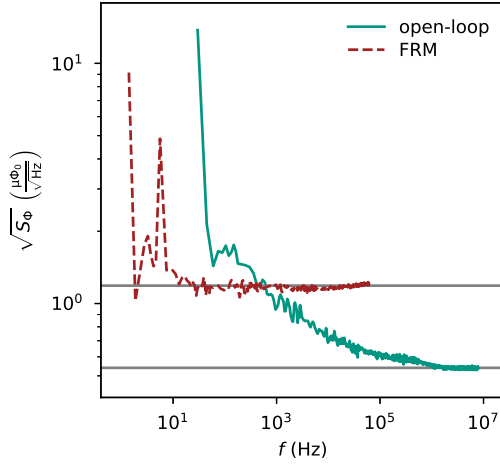


FIG. 11. Square root of the flux noise spectral density $\sqrt{S_{\Phi}(f)}$ for both open-loop and FRM readout of the same μ MUX device. Grey lines mark the white noise level at high frequencies.

B. Noise shaping

Compared to open-loop readout, flux ramp modulation has a significant effect on the shape of the magnetic flux noise spectral density. At high frequencies, the latter is typically dominated by white noise caused by cryogenic amplifiers. As flux ramp modulation leads to a reduced effective flux-to-transmission transfer coefficient $K_{\text{phi}}(\Phi) = (\partial |S_{21}(\Phi)| / \partial \Phi)$ as compared to open-loop readout, the white noise level is in general increased by a factor $c_{\text{deg}} > \sqrt{2}$ when using flux ramp modulation¹⁹. At low frequencies a $1/f^{\alpha}$ -like noise contribution due to two-level systems in the vicinity of the microwave resonator has been observed²⁷ dominating the overall noise spectral density at low frequency. Due to the nature of the flux ramp modulation, an offset of the transmission signal constant on timescales of the ramp reset rate f_{ramp} has no effect on the extracted phase. As a result, TLS noise contributions at frequencies of the order of the ramp reset rate f_{ramp} and below do (to first order) not contribute to the overall readout flux noise. Thus, flux ramp modulation can, at least partially, suppress the $1/f^{\alpha}$ -like noise contribution due to TLS. Despite the mathematical complexity of μ MUX and the FRM method, the simulation framework allows for a detailed prediction of the resulting readout flux noise spectral density.

Figure 11 shows the square root of the noise spectral density $\sqrt{S_{\Phi}(f)}$ of an example microwave SQUID multiplexer assuming open-loop and FRM readout. Both, a white amplifier noise with a noise temperature of $T_{\text{N}} = 4\text{K}$ and a $1/\sqrt{f}$ -like TLS noise with a noise level of $\sqrt{S_{\text{TLS}}}/f_{\text{res},0} = 2.5 \times 10^{-9} 1/\sqrt{\text{Hz}}$ at a frequency of 1 Hz were assumed for the simulations. These values serve as rough exemplary values for microresonators^{27,28}. For open-loop readout, the bias flux Φ_{bias} was chosen such that the flux-to-transmission transfer coefficient $K_{\text{phi}}(\Phi_{\text{bias}})$ is maximized. For FRM readout, a modulation ramp inducing at most one flux quantum into the SQUID loop with a ramp repetition rate of $f_{\text{ramp}} = f_s/128 \approx$

122 kHz was used. Due to the reduction in output sampling rate caused by the demodulation during FRM readout, the square root of the noise spectral density of open-loop readout extends to higher frequencies. At high frequencies where the curves are flat, FRM leads to a higher level of noise compared to open-loop readout by a factor of $c_{\text{deg}} = 2.18$. This is caused by the reduced effective gain as discussed before. In the case of open-loop readout, the noise contribution due to two-level systems results in a characteristic increase of the square root of the noise spectral density towards low frequencies. As expected, this increase is significantly less prominent for FRM readout, where the noise spectral density is mostly white. Low-frequency noise added in the signal chain after the SQUID is hence significantly reduced, however due to nonlinearities not fully removed. As a result at frequencies around 10 Hz and below, a slight increase of the noise level towards low frequencies is visible even for FRM readout. Similar analysis can help to further investigate the effects that readout schemes like FRM have on the noise of μ MUX and may ultimately lead to an improved understanding of the intricate behavior of such devices.

VIII. CONCLUSION

We presented a simulation framework based on a Monte-Carlo method to simulate the characteristics and performance of a single channel of a microwave SQUID multiplexer. Our simulation framework is based on the state-of-the-art multiplexer model including a full description of the dependence of device performance on the screening parameter β_{L} and the rf flux amplitude Φ_{rf} as well as dynamical effects due to the finite bandwidth of the microwave resonator. Either open-loop or FRM readout can be used for the simulation. To verify that the software works as intended, we performed several sanity checks and showed that our simulation results are in excellent agreement with experimental results. Moreover, we showed that it allows resembling the expected behavior of more sophisticated devices such as hybrid microwave SQUID multiplexers as long as they are direct derivatives of a conventional μ MUX. We presented first steps towards a full optimization of microwave SQUID multiplexers by exploring the dependence of μ MUX performance on a small subset of all possible device and readout parameters. We showed, for example, that device performance is better in case that the probe tone frequency is larger than the unloaded resonance frequency $f_{\text{exc}} > f_{\text{res},0}$ and that a value of the SQUID hysteresis parameter in the range $0.3 \leq \beta_{\text{L}} \leq 0.5$ yields the minimum magnetic flux noise. Moreover, we showed that the probe tone power P_{exc} should be chosen such that a rf flux amplitude $\Phi_{\text{rf}} = 0.3\Phi_0$ is threading the SQUID loop and that the typical choice of $\eta_0 = 1$ is not universal, and that $\eta_0 > 1$ can result in a lower minimum readout noise at a lower probe tone power. The latter can significantly improve the multiplexing factor in systems limited by the cryogenic amplifier IIP3 point. Finally, we highlighted other applications of our simulation framework such as a discussion of linearity or noise shaping.

ACKNOWLEDGMENTS

This work was performed within the framework of the DFG research unit FOR 2202 (funding under grant no. En299/7-1 and En299/7-2). C. Schuster further gratefully acknowledges support by the Karlsruhe School of Elementary Particle and Astroparticle Physics: Science and Technology (KSETA).

DATA AVAILABILITY STATEMENT

The data that support the findings of this study are available from the corresponding author upon reasonable request.

REFERENCES

- ¹K. D. Irwin and G. C. Hilton, *Topics Appl. Phys.*, edited by C. Enss, 2005 (2005) pp. 63–149.
- ²J. N. Ullom and D. A. Bennett, “Review of superconducting transition-edge sensors for x-ray and gamma-ray spectroscopy,” *Superconductor Science and Technology* **28**, 084003 (2015).
- ³A. Fleischmann, C. Enss, and G. Seidel, “Metallic magnetic calorimeters,” (2005) pp. 197–211.
- ⁴S. Kempf, A. Fleischmann, L. Gastaldo, and C. Enss, “Physics and Applications of Metallic Magnetic Calorimeters,” *Journal of Low Temperature Physics* , 1–15 (2018).
- ⁵P. C. Nagler, J. S. Adams, M. A. Balvin, S. R. Bandler, K. L. Denis, W. T. Hsieh, D. P. Kelly, J. P. Porst, J. E. Sadleir, G. M. Seidel, S. J. Smith, and T. R. Stevenson, “Performance of magnetic penetration thermometers for x-ray astronomy,” *Journal of Low Temperature Physics* **167**, 455–460 (2012).
- ⁶S. R. Bandler, K. D. Irwin, D. Kelly, P. N. Nagler, J. P. Porst, H. Rotzinger, J. E. Sadleir, G. M. Seidel, S. J. Smith, and T. R. Stevenson, “Magnetically coupled microcalorimeters,” *Journal of Low Temperature Physics* **167**, 254–268 (2012).
- ⁷R. L. Fagaly, “Superconducting quantum interference device instruments and applications,” *Review of Scientific Instruments* **77**, 101101 (2006), <https://doi.org/10.1063/1.2354545>.
- ⁸W. B. Doriese, K. M. Morgan, D. A. Bennett, E. V. Denison, C. P. Fitzgerald, J. W. Fowler, J. D. Gard, J. P. Hays-Wehle, G. C. Hilton, K. D. Irwin, Y. I. Joe, J. A. B. Mates, G. C. O’Neil, C. D. Reintsema, N. O. Robbins, D. R. Schmidt, D. S. Swetz, H. Tatsuno, L. R. Vale, and J. N. Ullom, “Developments in Time-Division Multiplexing of X-ray Transition-Edge Sensors,” *Journal of Low Temperature Physics* **184**, 389–395 (2016).
- ⁹R. H. den Hartog, M. P. Bruijn, A. Clenet, L. Gottardi, R. Hijmering, B. D. Jackson, J. van der Kuur, B. J. van Leeuwen, A. J. van der Linden, D. van Loon, A. Nieuwenhuizen, M. Ridder, and P. van Winden, “Progress on the FDM Development at SRON: Toward 160 Pixels,” *Journal of Low Temperature Physics* **176**, 439–445 (2014).
- ¹⁰D. Richter, L. Hoibl, T. Wolber, N. Karcher, A. Fleischmann, C. Enss, M. Weber, O. Sander, and S. Kempf, “Flux ramp modulation based mhz frequency-division dc-squid multiplexer,” *Applied Physics Letters* **118**, 122601 (2021), <https://doi.org/10.1063/5.0044444>.
- ¹¹J. A. B. Mates, G. C. Hilton, K. D. Irwin, L. R. Vale, and K. W. Lehnert, “Demonstration of a multiplexer of dissipationless superconducting quantum interference devices,” *Applied Physics Letters* **92**, 023514 (2008), <https://doi.org/10.1063/1.2803852>.
- ¹²F. Hirayama, S. Kohjiro, D. Fukuda, H. Yamamori, S. Nagasawa, and M. Hidaka, “Microwave squid multiplexer for tes readout,” *IEEE Transactions on Applied Superconductivity* **23**, 2500405–2500405 (2013).
- ¹³S. Kempf, M. Wegner, L. Deeg, A. Fleischmann, L. Gastaldo, F. Herrmann, D. Richter, and C. Enss, “Design, fabrication and characterization of a 64 pixel metallic magnetic calorimeter array with integrated, on-chip microwave SQUID multiplexer,” *Superconductor Science and Technology* **30** (2017), 10.1088/1361-6668/aa6d17.
- ¹⁴K. M. Morgan, B. K. Alpert, D. A. Bennett, E. V. Denison, W. B. Doriese, J. W. Fowler, J. D. Gard, G. C. Hilton, K. D. Irwin, Y. I. Joe, G. C. O’Neil, C. D. Reintsema, D. R. Schmidt, J. N. Ullom, and D. S. Swetz, “Code-division-multiplexed readout of large arrays of tes microcalorimeters,” *Applied Physics Letters* **109**, 112604 (2016), <https://doi.org/10.1063/1.4962636>.
- ¹⁵C. D. Reintsema, J. Beall, W. Doriese, W. Duncan, L. Ferreira, G. C. Hilton, K. D. Irwin, D. Schmidt, J. Ullom, L. Vale, and Y. Xu, “A tdma hybrid squid multiplexer,” *Journal of Low Temperature Physics* **151**, 927–933 (2008).
- ¹⁶K. D. Irwin, S. Chaudhuri, H. M. Cho, C. Dawson, S. Kuenstner, D. Li, C. J. Titus, and B. A. Young, “A spread-spectrum squid multiplexer,” *Journal of Low Temperature Physics* **193**, 476–484 (2018).
- ¹⁷C. Yu, A. Ames, S. Chaudhuri, C. Dawson, K. D. Irwin, S. E. Kuenstner, D. Li, and C. J. Titus, “An impedance-modulated code-division microwave squid multiplexer,” *Engineering Research Express* **2** (2020), 10.1088/2631-8695/ab68a4.
- ¹⁸C. Schuster, M. Wegner, C. Enss, and S. Kempf, “Flux ramp modulation based hybrid microwave squid multiplexer,” *Applied Physics Letters* **120**, 162601 (2022), <https://doi.org/10.1063/5.0087994>.
- ¹⁹J. A. Mates, K. D. Irwin, L. R. Vale, G. C. Hilton, J. Gao, and K. W. Lehnert, “Flux-ramp modulation for SQUID multiplexing,” *Journal of Low Temperature Physics* **167**, 707–712 (2012).
- ²⁰M. Wegner, C. Enss, and S. Kempf, “Analytical model of the readout power and SQUID hysteresis parameter dependence of the resonator characteristics of microwave SQUID multiplexers,” *Superconductor Science and Technology* **35**, 075011 (2022).
- ²¹P. D. Welch, “The use of fast fourier transform for the estimation of power spectra: A method based on time averaging over short, modified periodograms,” *IEEE Transactions on Audio and Electroacoustics* **15**, 70–73 (1967).
- ²²L. Gastaldo, K. Blaum, K. Chrysalidis, T. Day Goodacre, A. Domula, M. Door, H. Dorrer, C. E. Düllmann, K. Eberhardt, S. Eliseev, C. Enss, A. Faessler, P. Filianin, A. Fleischmann, D. Fonnesu, L. Gamer, R. Haas, C. Hassel, D. Hengstler, J. Jochum, K. Johnston, U. Keschull, S. Kempf, T. Kieck, U. Köster, S. Lahiri, M. Maiti, F. Mantegazzini, B. Marsh, P. Neroutsos, Y. N. Novikov, P. C. Ranitzsch, S. Rothe, A. Rischka, A. Saenz, O. Sander, F. Schneider, S. Scholl, R. X. Schüssler, C. Schweiger, F. Simkovic, T. Stora, Z. Szücs, A. Türler, M. Veinhard, M. Weber, M. Wegner, K. Wendt, and K. Zuber, “The electron capture in 163Ho experiment – ECHO,” *European Physical Journal: Special Topics* **226**, 1623–1694 (2017).
- ²³M. Wegner, N. Karcher, O. Krömer, D. Richter, F. Ahrens, O. Sander, S. Kempf, M. Weber, and C. Enss, “Microwave SQUID Multiplexing of Metallic Magnetic Calorimeters: Status of Multiplexer Performance and Room-Temperature Readout Electronics Development,” *Journal of Low Temperature Physics* **193**, 462–475 (2018).
- ²⁴N. Karcher, D. Richter, F. Ahrens, R. Gartmann, M. Wegner, O. Krömer, S. Kempf, C. Enss, M. Weber, and O. Sander, “Sdr-based readout electronics for the echo experiment,” *Journal of Low Temperature Physics* **200** (2020), 10.1007/s10909-020-02463-w.
- ²⁵J. A. B. Mates, D. T. Becker, D. A. Bennett, B. J. Dober, J. D. Gard, J. P. Hays-Wehle, J. W. Fowler, G. C. Hilton, C. D. Reintsema, D. R. Schmidt, D. S. Swetz, L. R. Vale, and J. N. Ullom, “Simultaneous readout of 128 x-ray and gamma-ray transition-edge microcalorimeters using microwave squid multiplexing,” *Applied Physics Letters* **111**, 062601 (2017), <https://doi.org/10.1063/1.4986222>.
- ²⁶S. Henderson, Z. Ahmed, J. Austermann, D. Becker, D. Bennett, D. M. Brown, S. Chaudhuri, H. Cho, J. D’Ewart, B. Dober, S. Duff, J. Dusatko, S. Fatigoni, J. Frisch, J. D. Gard, M. Halpern, G. Hilton, J. Hubmayr, K. Irwin, E. Karpel, S. S. Kernasovskiy, S. Kuenstner, C. Kuo, D. Li, J. A. B. Mates, C. Reintsema, S. Smith, J. Ullom, L. Vale, D. D. V. Winkle, M. Vissers, and C. Yu, “Highly-multiplexed microwave squid readout using the slac microresonator radio frequency (smurf) electronics for future cmb and sub-millimeter surveys,” in *Astronomical Telescopes + Instrumentation* (2018).

²⁷J. Gao, J. Zmuidzinas, B. A. Mazin, H. G. LeDuc, and P. K. Day, "Noise properties of superconducting coplanar waveguide microwave resonators," *Applied Physics Letters* **90**, 102507 (2007), <https://doi.org/10.1063/1.2711770>.

²⁸We are aware that the TLS noise power depends on both probe tone power and resonator geometry, and chose these values purely to showcase the

functionality of the simulation software. In a future iteration of the simulation framework, a full model for TLS noise may be included.